Electronic Supplementary Information

Regulating the coordination microenvironment of zinc single-atom catalysts to enhance intramolecular hydroamination performance

Li Wang,[a,c] Chao Lv,[a,c] Kecan Dou,[a] Deqiong Xie,[a] Yanghe Fu,[a,b] Fumin Zhang,[a,b]* De-Li Chen,[a,b]* and Weidong Zhu[a,b]*

[a]Key Laboratory of the Ministry of Education for Advanced Catalysis Materials, Institute of Physical Chemistry, Zhejiang Normal University, Jinhua 321004, People's Republic of China

[b]Zhejiang Engineering Laboratory for Green Syntheses and Applications of Fluorine-Containing Specialty Chemicals, Institute of Advanced Fluorine-Containing Materials, Zhejiang Normal University, Jinhua 321004, People's Republic of China.

[c]These authors contributed equally to this work

***Corresponding Authors:**

Fumin Zhang: zhangfumin@zjnu.edu.cn;

De-Li Chen: chendl@zjnu.cn;

Weidong Zhu: weidongzhu@zjnu.cn

Characterizations

The powder X-ray diffraction (XRD) patterns were acquired via a D8 Advance powder X-ray diffractometer using Cu *Kα* radiation (λ = 0.154 nm, operation voltage = 40 kV, operation current = 40 mA) ranging from the 2-theta range of 5° to 80°.

N_2 adsorption-desorption isotherm measurements were obtained on a Micromeritics ASAP 2020 apparatus at 77 K and up to 1 bar. Samples were degassed under vacuum at 473 K for 15 h prior to the adsorption measurement. The Brunauer-Emmet-Teller method was used to determine the specific surface areas in the relative pressure range of P/P_0 = 0.05 to 0.30. Density functional theory was used to calculate the pore size curves based on the adsorption isotherms, and the *t*-plot method was used to calculate the pore volume.

On a Thermo VG ESCALAB250, X-ray photoelectron spectroscopy (XPS) was carried out with a 300 W Al K radiation. The binding energies were measured with respect to the C1s line of adventitious carbon, which had a reference energy of 284.8 eV, and the base pressure was roughly 3×10^{-9} mbar.

Scanning electron microscopy (SEM) and transmission electron microscopy (TEM) images were conducted on a Hitachi S-4800 field emission and JEM2100F apparatus with an accelerating voltage ranging from 3 to 5 kV and 200 kV, respectively.

Transmission electron microscopy (TEM) images were measured on the JEM2100F device operating at 200 kV and elemental mapping analyses of energy dispersive X-ray (EDX) spectroscopy was applied to verify the existence and distribution of Zn, C, N, P, B, and S species.

Aberration-corrected high-angle annular dark-field scanning transmission electron microscopy (HAADF-STEM) measurements were measured by a FEI Themis Z instrument at 200 keV.

Raman spectroscopy was carried out using the InVia-Renishaw apparatus and a 532 nm

laser source.

Inductively coupled plasma atomic emission spectroscopy was used to measure the amounts of metal Zn in diverse materials (ICP-AES, iCAP 7400, Thermo, USA). In a quartz vessel, samples (30 mg) and aqua regia (5 mL) were mixed according to a standard procedure. The solution was processed in a microwave digester for 30 min at 493 K. The solution was then transferred to a beaker and refluxed for 72 h. After cooling, the solution was added into a 10 mL volumetric flask and diluted to 10 mL with deionized water.

X-ray absorption fine structure spectra (XAFS) were collected using a bench-top easyXAFS300+ instrument (easyXAFS, LLC). Spectra were collected using Si and Ge spherically bent crystal analyzers and Ag anode X-ray tube. Spectra were deadtime corrected and the energy was calibrated using foils standard.

Kinetic studies

The experiments utilized a total solution volume of 2 mL in a Schlenk tube with a capacity of 10 mL. Specifically, following the dissolution of 20 mg catalyst in 2 mL of toluene, 0.05 mmol of 2-(2-phenylethynyl)aniline was added. The reactor temperature was then set to a specific value, such as 353, 363, or 373 K, and maintained for 30 min. Afterwards, the catalytic reaction began via vigorous stirring at 700 rpm. The analysis of the reaction mixture with GC-FID revealed the extent of 2-(2-phenylethynyl)aniline conversion (x). The conversion (x) was subsequently used to calculate the ln(1-x) plot versus reaction time (min), enabling the extraction of pseudo-first-order rate constants (k) from the slope (Equation (1)). The Arrhenius equation using data points controlled below 25% of 2-(2-phenylethynyl)aniline conversions was utilized to estimate the activation energy (E_a) for the reaction (Equation (2)). In this case, k refers to the rate constant at temperature T (K), and A and E_a refer to the Arrhenius factor and activation energy, respectively.

$$-ln(1-x) = kt \qquad (1)$$

$$ln\,k = ln\,A - E_a/RT \qquad (2)$$

Theoretical section

Spin polarized density functional theory-based method as implemented in the Vienna *ab* initio Simulation Package (VASP)[s1-4] was employed for all of the calculations in this study. Slab models were constructed on a graphene sheet to simulate the metal single atom catalysts. The projector augmented wave (PAW) method was employed to describe the interaction between electrons and ions. The electron exchange-correlation energies were computed within the generalized gradient approximation method (GGA) using the Perdew-Burke-Ernzerhof (PBE) functional.[s5] To account for the weak van der Waals interaction, the DFT-D3 scheme[s6] was applied. The dipole correction was included along the z direction of the slab. A supercell with dimensions of $a = b = 14.76$ Å was utilized to represent the graphene sheet-based catalysts, and a vacuum of 18.0 Å along the z-direction. A kinetic cutoff energy of 500 eV was applied, and the optimization was considered converged only when the energy difference was less than 10^{-5} eV and the absolute force for each ion in the system was smaller than 0.03 eV/Å. The Brillouin zone was sampled using a Monkhorst-Pack grid with a *k*-point of 3×3×1. The adsorption energy (E_{ads}) was calculated as

$$E_{ads} = E_{molecule/slab} + E_{slab} - E_{molecule} \qquad (1)$$

where the $E_{molecule/slab}$, E_{slab}, and $E_{molecule}$ represent the total energy of the slab with adsorbed molecule, slab model, and isolated molecule in the gas phase, respectively. Therefore, a more negative adsorption energy indicates a stronger interaction between the adsorbate and the surface. The climbing-image nudged elastic band (CI-NEB) method[s7] was utilized to locate the transition states, and the validity of these states was confirmed by ensuring they possessed only one imaginary frequency. In addition, the Bader charge analysis were conducted to assess the electron population in specific systems. The corrected Gibbs free energies[s8] at 373 K for the intermediates and transition states in the reaction profiles were calculated by

$$E_{\text{Gibbs}} = \text{ZPE} + U_{\text{vib}} - TS_{vib} \quad (2)$$

where the ZPE denotes the zero-point energy, and only vibrational modes were considered to account for the internal energy U_{vib} and entropy S_{vib}.

Table S1 Textural properties and zinc contents of the prepared catalysts

Sample	S_{BET}[a] (m^2/g)	V_{total} (cm^3/g)	Zn[b] (wt.%)
Zn-N_3	1049.9	2.17	2.4
Zn-N_2P	1534.0	1.99	1.8
Zn-N_2B	1173.9	1.46	2.0
Zn-N_2S	1344.6	1.59	3.9

[a]By BET method. [b]by ICP−AES analysis.

Table S2 Non-metallic element contents in the prepared catalysts

Sample	Relative concentrations of different element (wt.%)		
	P[a]	**B**[a]	**S**[b]
Zn-N_2P	2.0		
Zn-N_2B		2.5	
Zn-N_2S			2.8

[a]By ICP−AES analysis, [b]by elemental analysis.

Table S3 Total nitrogen content and the relative concentrations of the various nitrogen species present in the prepared catalysts

Sample	Total N (atom%)	Relative concentrations of different N species (area%)				
		Pyridinic N	$Zn\text{-}N_x$	Pyrrolic N	Graphitic N	N-oxide
$Zn\text{-}N_3$	4.2	21.0	9.3	7.5	26.0	36.2
$Zn\text{-}N_2P$	6.9	14.5	21.1	19.2	20.3	24.9
$Zn\text{-}N_2B$	8.5	27.1	19.1	12.8	14.7	26.3
$Zn\text{-}N_2S$	7.8	19.7	17.2	13.1	23.1	26.9

Table S4 Structural parameters of different samples extracted from the EXAFS fitting

Sample	Shell	CN	*R* (Å)	σ^2 (10^{-3} Å^2)	ΔE_0 (eV)	*R* factor
Zn foil	Zn-Zn	6 (fixed)	2.64 ± 0.01	10.6 ± 0.8	-0.3 ± 1.1	0.008
	Zn-Zn	6 (fixed)	3.25 ± 0.01	2.9 ± 5.8		
ZnO	Zn-O	6 (fixed)	2.14 ± 0.01	4.1 ± 1.6	4.3 ± 1.2	0.012
	Zn-Zn	12 (fixed)	3.03 ± 0.01	2.6 ± 2.1		
	Zn-O-Zn	24 (fixed)	3.59 ± 0.01	3.5 ± 3.9		
Zn-N_3	Zn-N	3.1 ± 0.1	1.95 ± 0.01	2.6 ± 3.9	1.0 ± 3.4	0.012
Zn-N_2P	Zn-N	1.9 ± 0.3	1.95 ± 0.01	1.9 ± 2.1	1.6 ± 4.4	0.016
	Zn-P	0.7 ± 0.2	2.08 ± 0.01	2.6 ± 3.4	2.4 ± 3.6	
Zn-N_2B	Zn-N	2.3 ± 0.2	1.94 ± 0.01	4.2 ± 6.5	-0.4 ± 2.7	0.015
	Zn-B	0.6 ± 0.2	2.14 ± 0.01	2.9 ± 1.6	3.9 ± 1.3	
Zn-N_2S	Zn-N	2.3 ± 0.3	1.95 ± 0.01	5.1 ± 6.3	1.8 ± 7.2	0.009
	Zn-S	1.2 ± 0.2	2.17 ± 0.01	1.6 ± 0.2	5.2 ± 3.7	

Data ranges: $3.0 \leq k \leq 12.5$ Å^{-1}, $1.2 \leq R \leq 4$ Å. R: bond distance; σ^2: Debye-Waller factors; *R* factor: goodness of fit. S_0^2 is the amplitude reduction factor (S_0^2 =0.82 was obtained by Zn foil fitting and applied for the other samples fitting)

Table S5 Kinetic parameters of intramolecular hydroamination over the prepared catalysts

Sample	T (K)	k (min^{-1})	E_a (kJ/mol)
	373	4.3×10^{-3}	
Zn-N_2P	363	2.0×10^{-3}	94.7 ± 3.3
	353	8.0×10^{-4}	
	373	2.0×10^{-3}	
Zn-N_3	363	8.7×10^{-4}	103.9 ± 1.7
	353	3.1×10^{-4}	
	373	9.3×10^{-4}	
Zn-N_2B	363	3.4×10^{-4}	123.7 ± 2.2
	353	1.0×10^{-4}	
	373	7.8×10^{-4}	
Zn-N_2S	363	2.7×10^{-4}	129.5 ± 1.7
	353	7.5×10^{-5}	

Table S6 Comparison of Zn-N_2P's catalytic activity versus analogous catalysts documented in literature, in the context of intramolecular hydroamination of 2-(2-phenylethynyl)aniline

Catalyst	Temperature (K)	Time (h)	Yield (%)	TOF (h^{-1})	Ref.
Ir(III)Cp*	323	1.5	90	12	s9
$NaAuCl_4 \cdot 2H_2O$	293	37	90	0.49	s10
Au/TiO_2	393	1	93	18.6	s11
$Pd\text{-}Fe_3O_4$	439	0.5	39	78	s12
Pt(II)-NaY	383	24	98	273	s13
CuI	383	15	63	0.04	s14
$Cu(OAc)_2 \cdot H_2O$	353	20	82	0.82	s15
$LiCB_{11}H_{12}$	393	24	84	0.18	s16
$ZnBr_2$		0.5	68	1.36	s17
Zn-UiO-67-BPY	373	24	100	0.24	s18
$Zn(II)/SiO_2$	363	24	98	0.68	s19
$Zn\text{-}N_2P$	373	10	100	3.62	**This work**

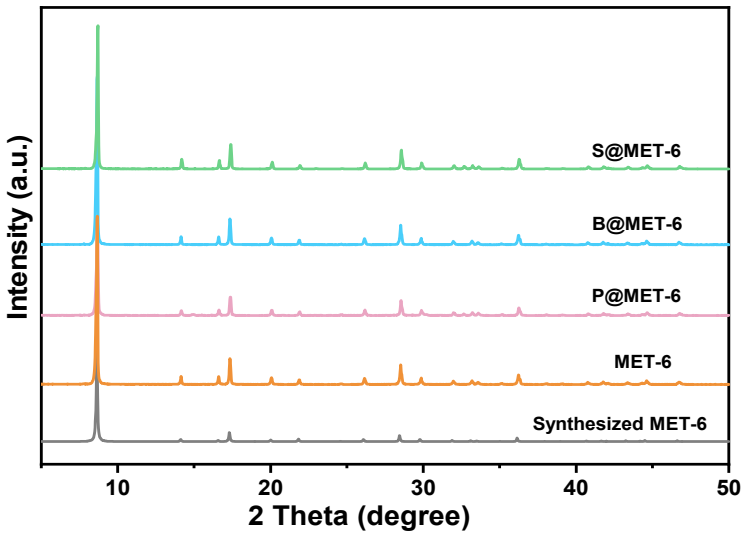

Figure S1. XRD patterns of various samples.

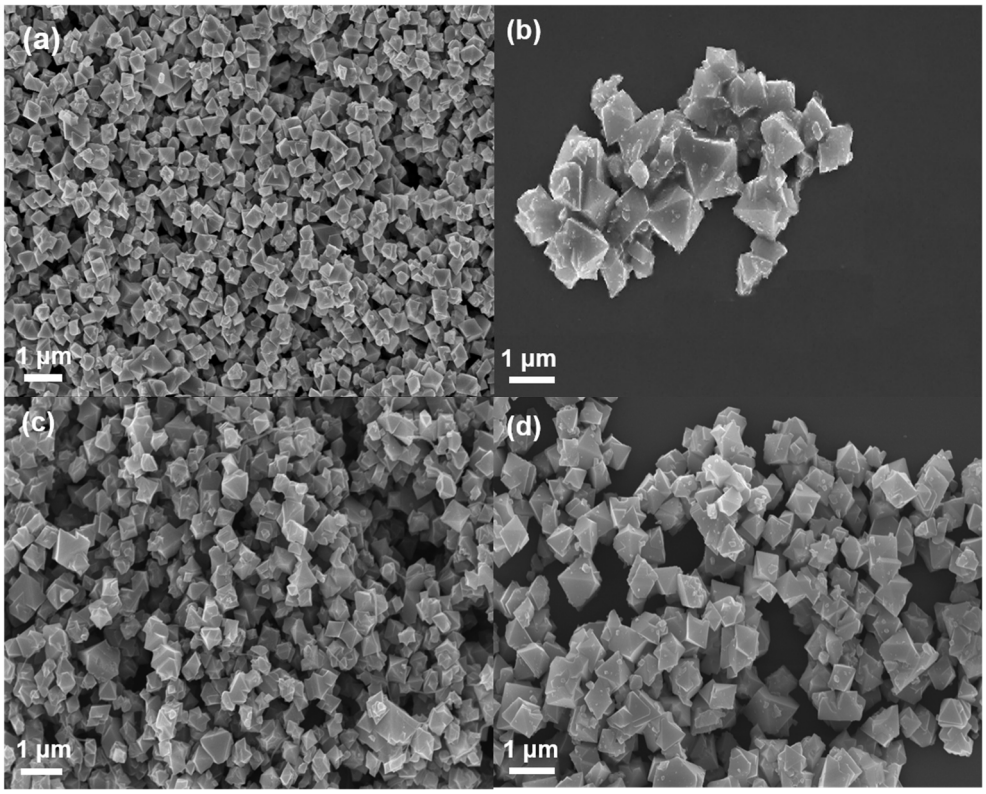

Figure S2. SEM images of MET-6 (a), S@MET-6 (b), B@MET-6 (c), and P@MET-6 (d).

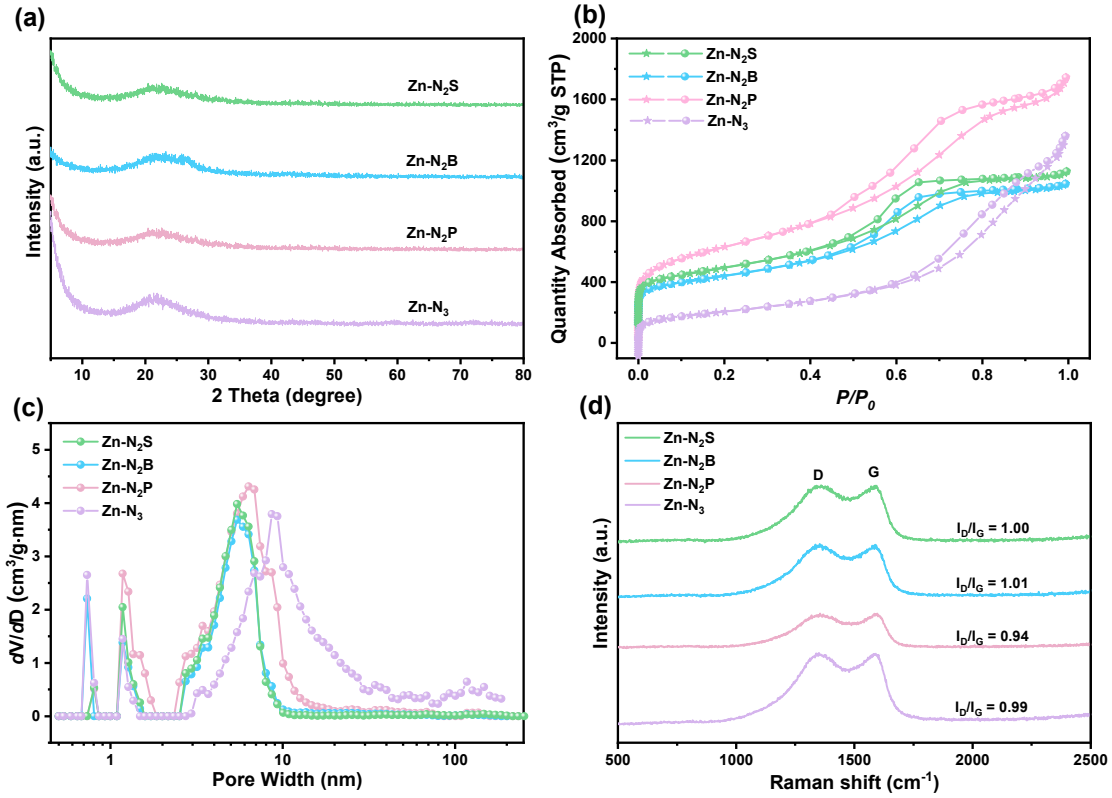

Figure S3. XRD patterns (a), N_2 adsorption-desorption isotherms at 77 K (b), pore size distributions (c), and Raman spectra (d) of Zn-N_2S, Zn-N_2B, Zn-N_2P and Zn-N_3 SACs.

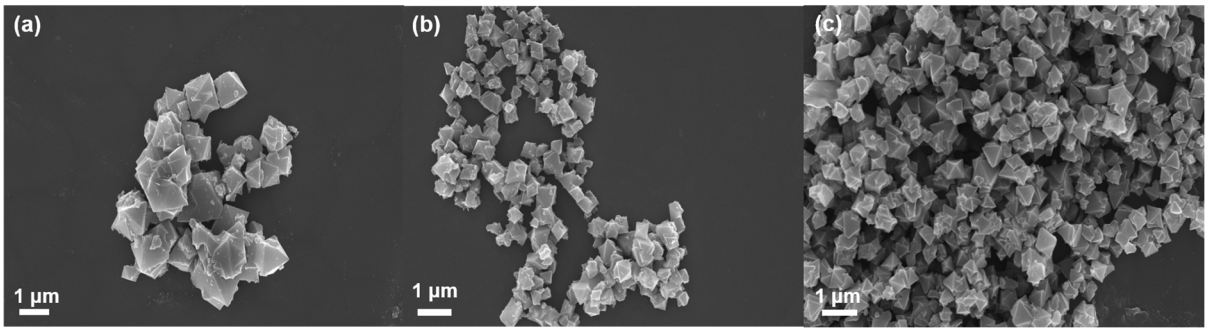

Figure S4. SEM images of Zn-N_2S (a), Zn-N_2B (b), and Zn-N_2P SACs (c).

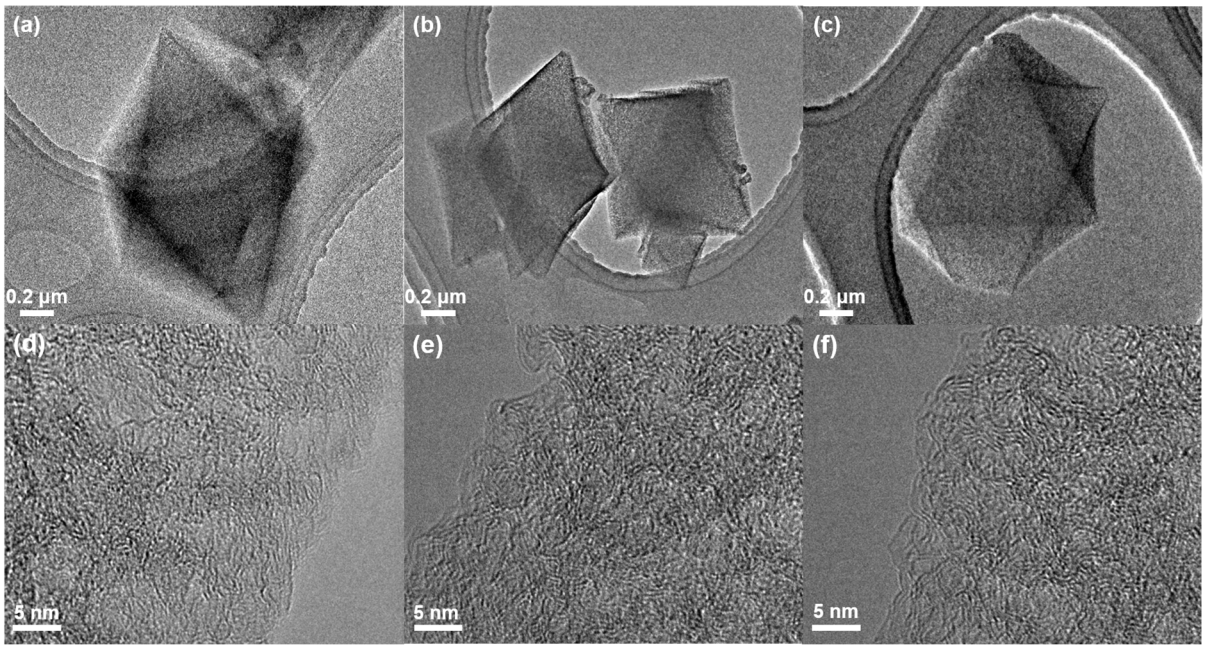

Figure S5. TEM images of Zn-N_2S (a, d), Zn-N_2B (b, e), and Zn-N_2P SACs (c, f).

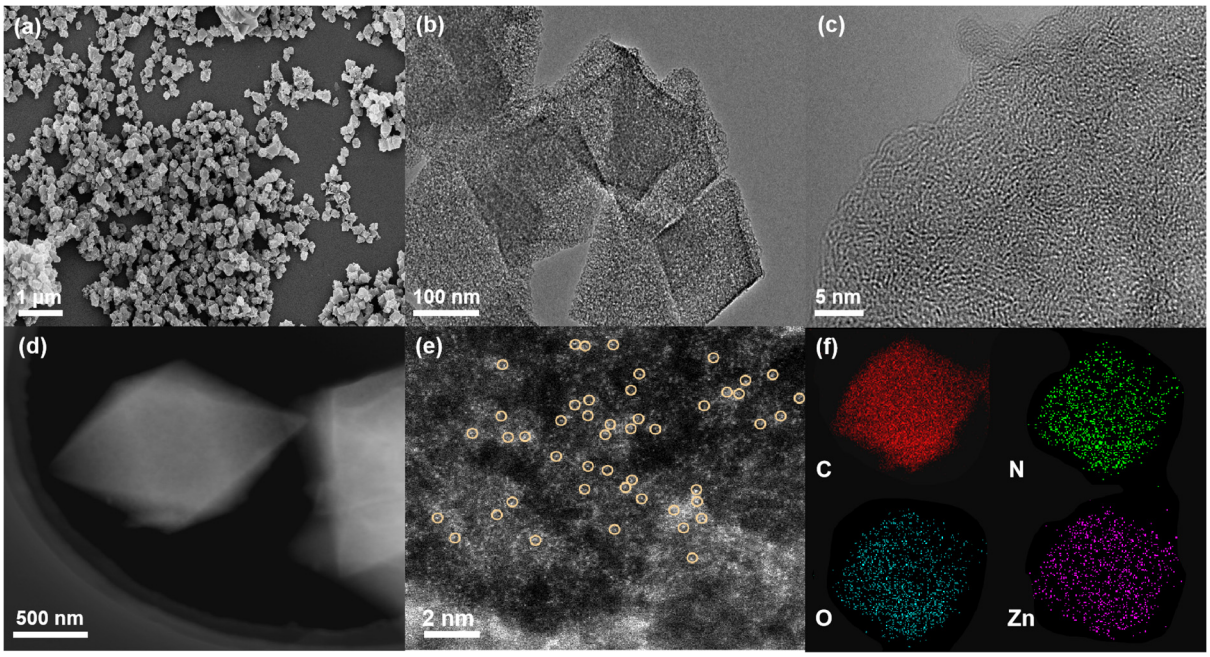

Figure S6. SEM (a), TEM (b), HRTEM (c), STEM (d), HAADF-STEM images (e) and the EDX elemental mappings (f) of Zn-N_3.

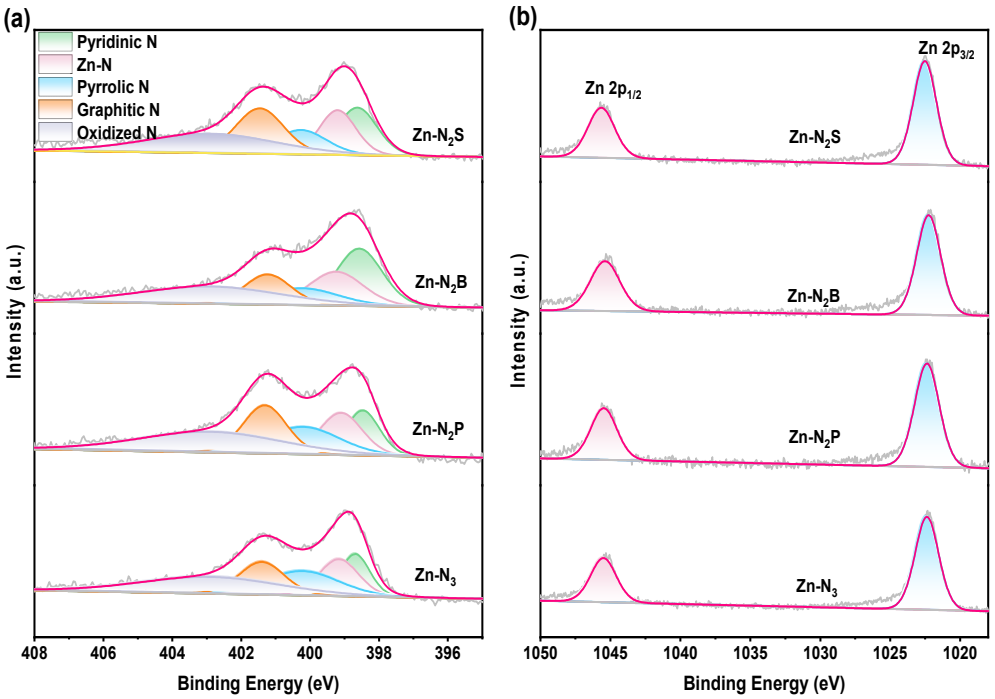

Figure S7. High-resolution N 1s XPS spectra (a) and Zn 2p XPS spectra (b) of Zn-N_2S, Zn-N_2B, Zn-N_2P, and Zn-N_3 SACs.

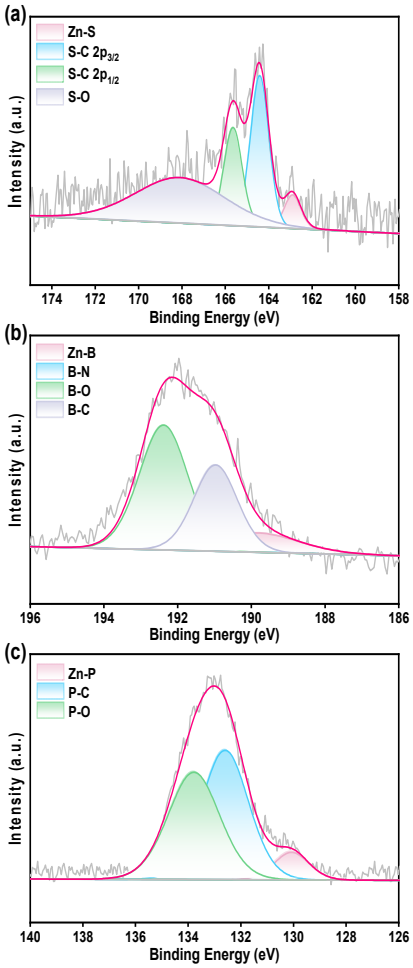

Figure S8. High-resolution S 2p XPS spectra of Zn-N_2S (a), B 1s XPS spectra of Zn-N_2B (b), and P 2p XPS spectra of Zn-N_2P (c).

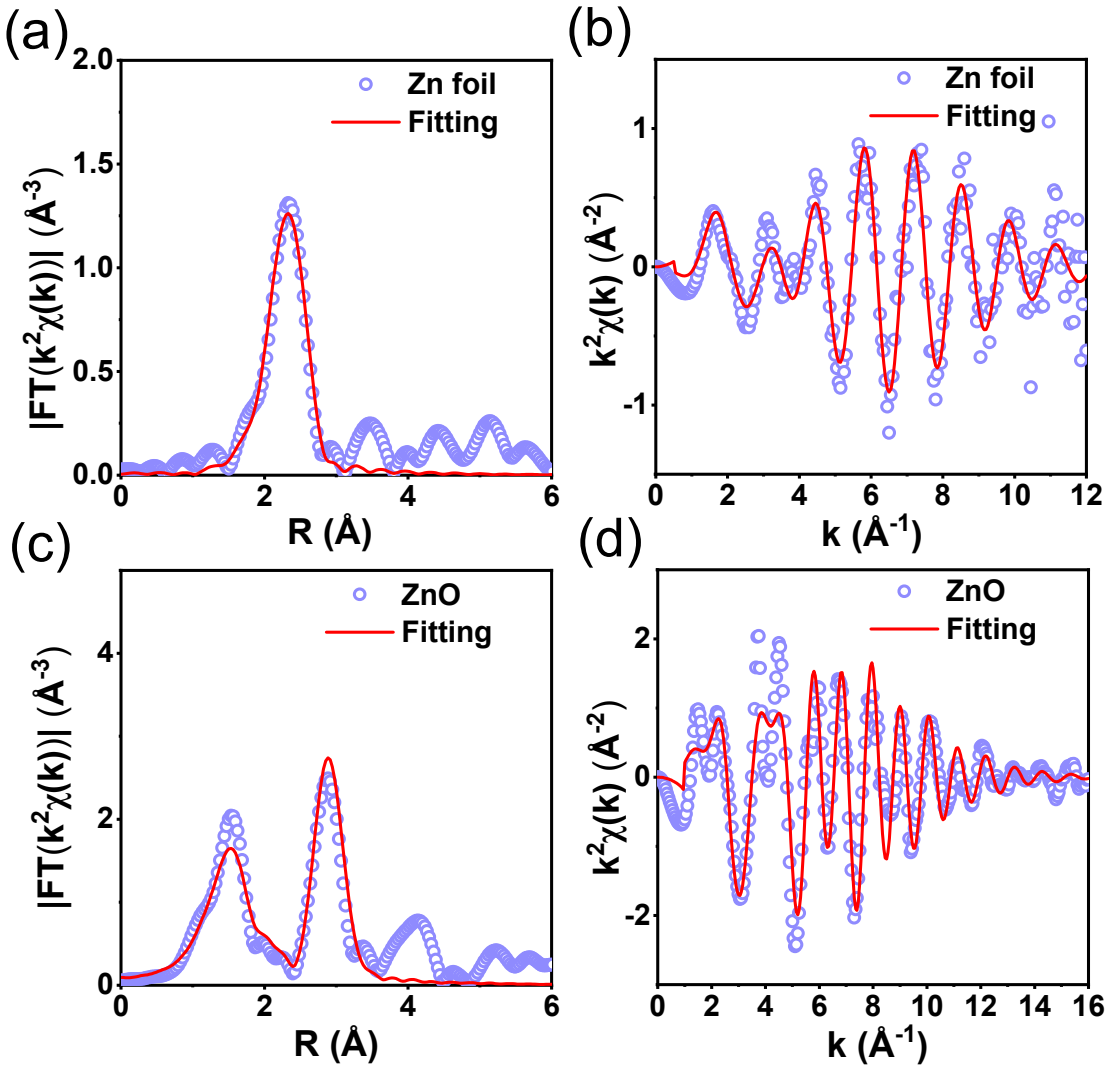

Figure S9. FT-EXAFS fitting curve of Zn foil in (a) *R* space, and (b) *k* space, and ZnO in (c) *R* space and (d) *k* space.

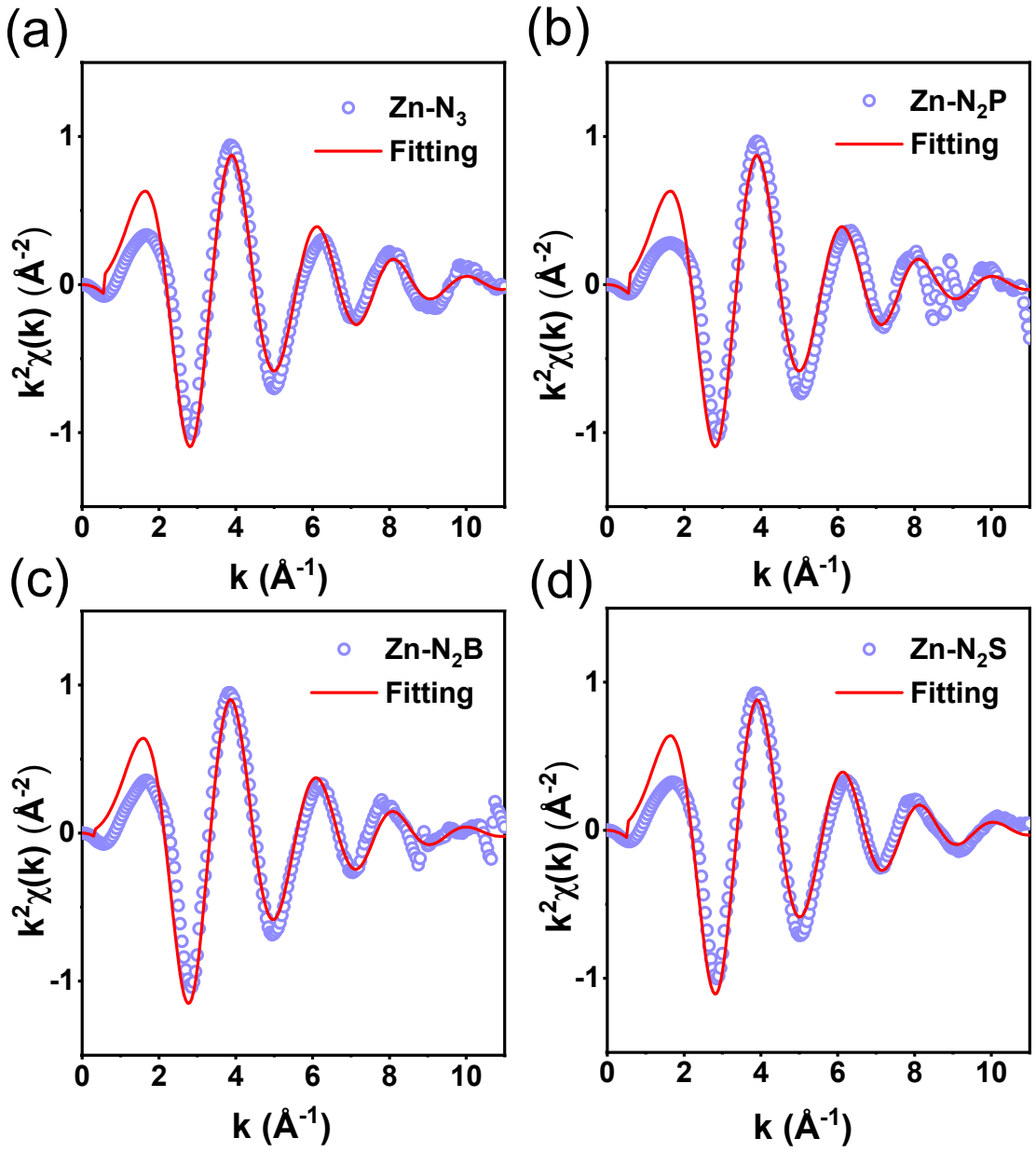

Figure S10. FT-EXAFS fitting curves of (a) Zn-N_3, (b) Zn-N_2P, (c) Zn-N_2B, and (d) Zn-N_2S in *k* space.

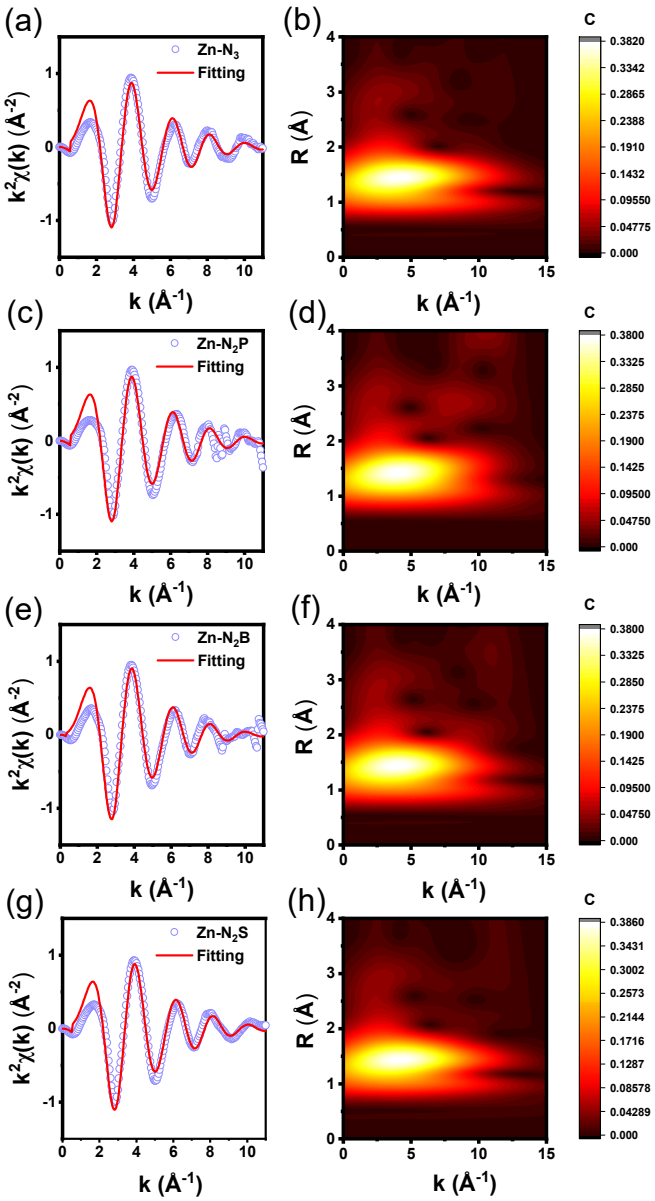

Figure S11. FT-EXAFS fitting curves in *k* space of (a) ZnN_3, (c) Zn-N_2P, (e) Zn-N_2B, and (g) Zn-N_2S. (b, d, f, and h) their corresponding wavelet-transformed k^3-weighted EXAFS spectra.

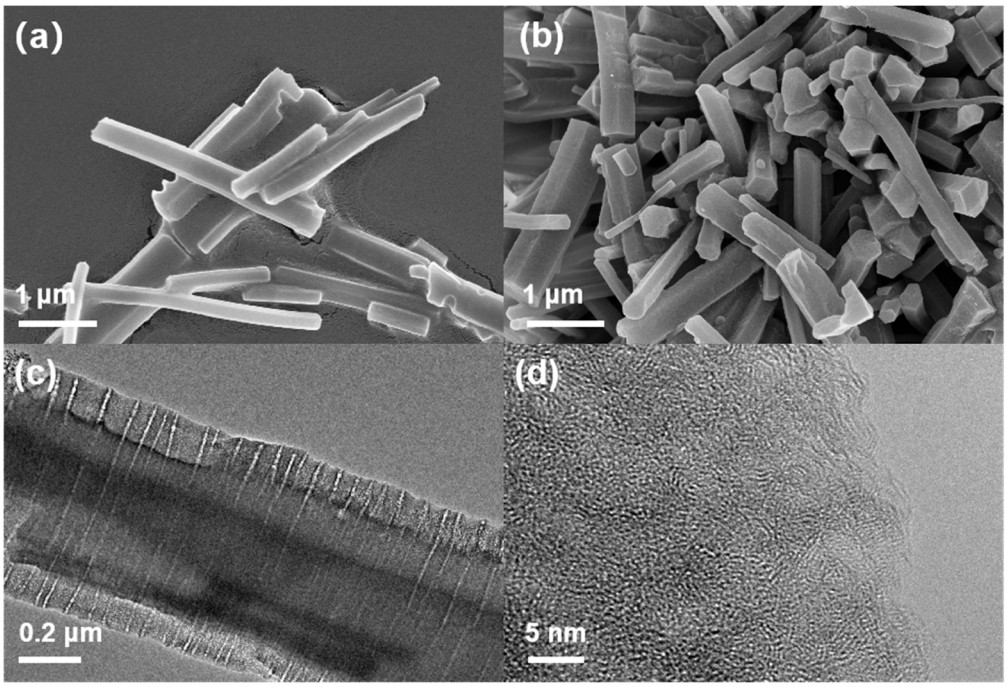

Figure S12. SEM images of Zn-MOF-74 (a) and the derived C (b). TEM and HRTEM images of derived C (c, d).

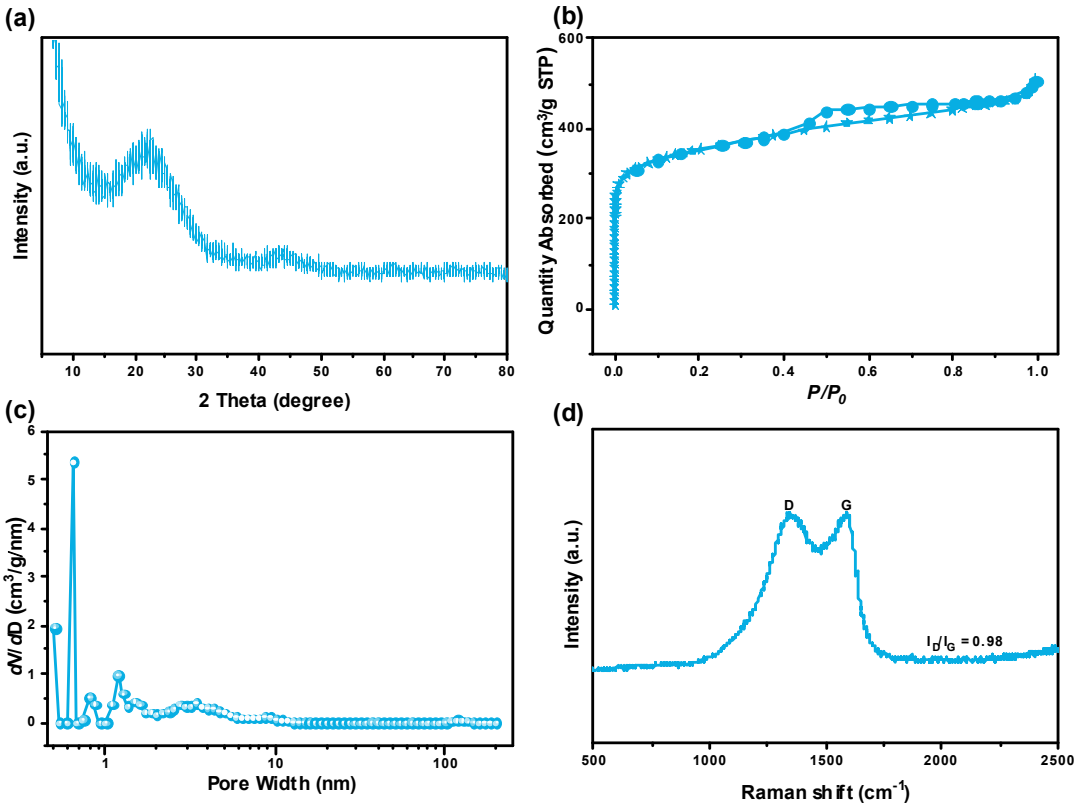

Figure S13. XRD pattern (a), Raman spectrum (b), N_2 adsorption-desorption isotherms at 77 K (c), and the pore size distributions of C (d).

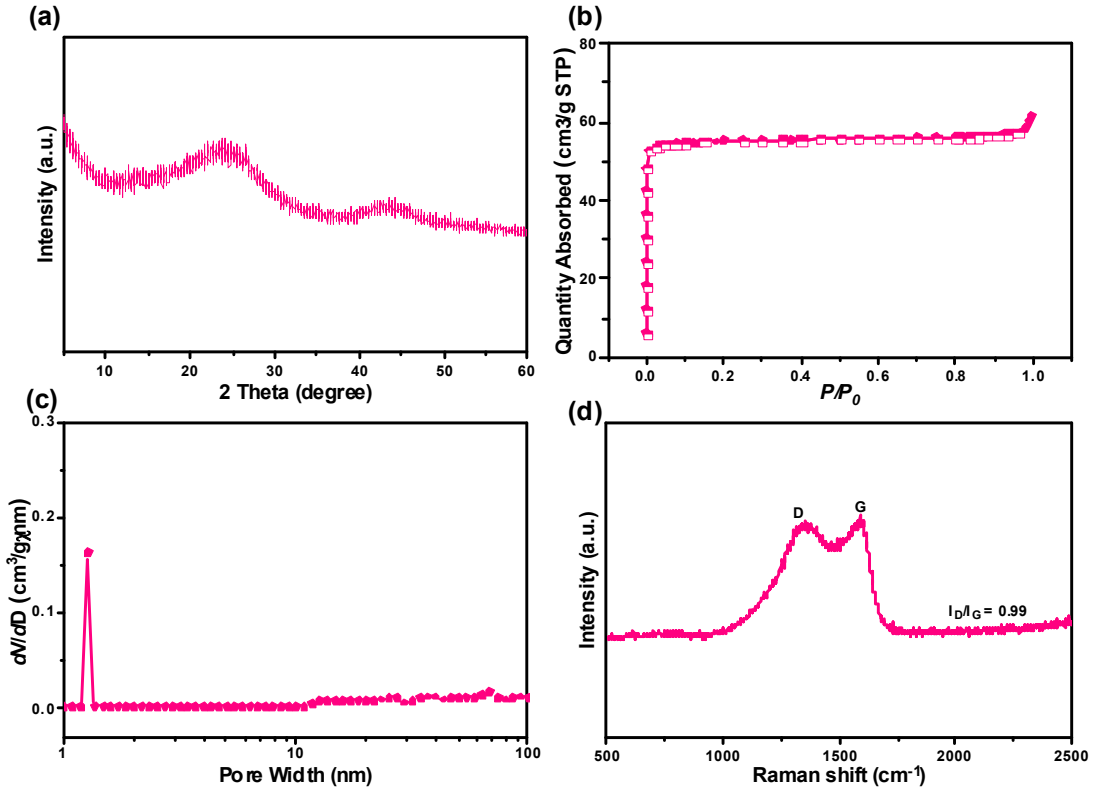

Figure S14. XRD pattern (a), N_2 adsorption-desorption isotherms at 77 K (b), pore size distributions (c), and the Raman spectrum (d) of NC.

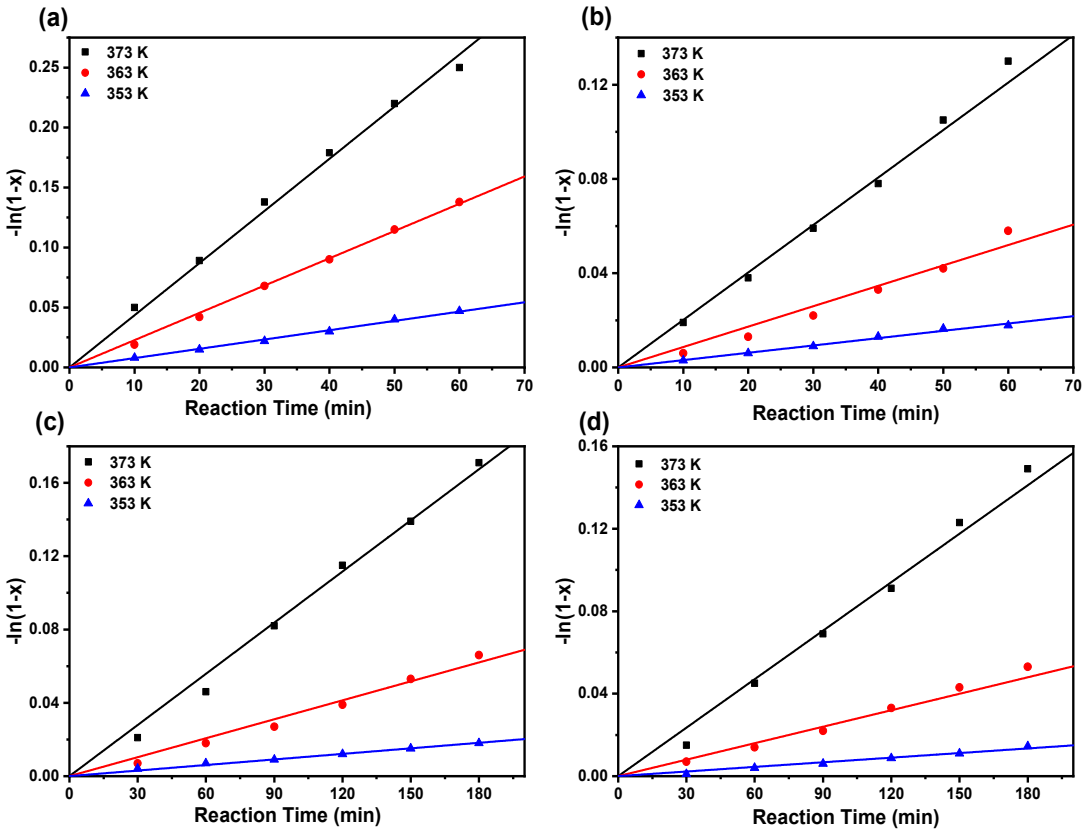

Figure S15. Plot of -ln(1-*x*) versus reaction time for the intramolecular hydroamination over (a) Zn-N_2P, (b) Zn-N_2, (c) Zn-N_2B, and (d) Zn-N_2S.

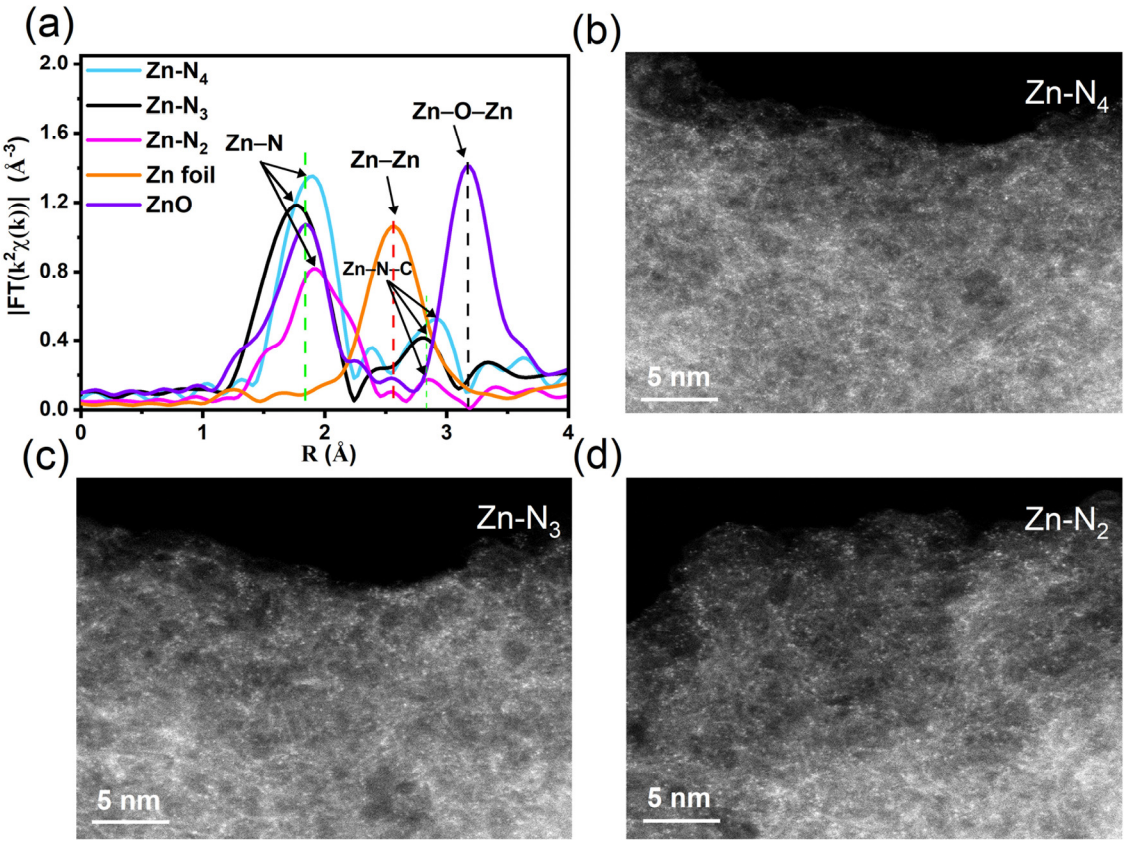

Figure S16. (a) FT of the k2-weighted EXAFS spectra of various samples, and HAADF-STEM of (b) Zn-N_4, (c) Zn-N_3, and (d) Zn-N_2.

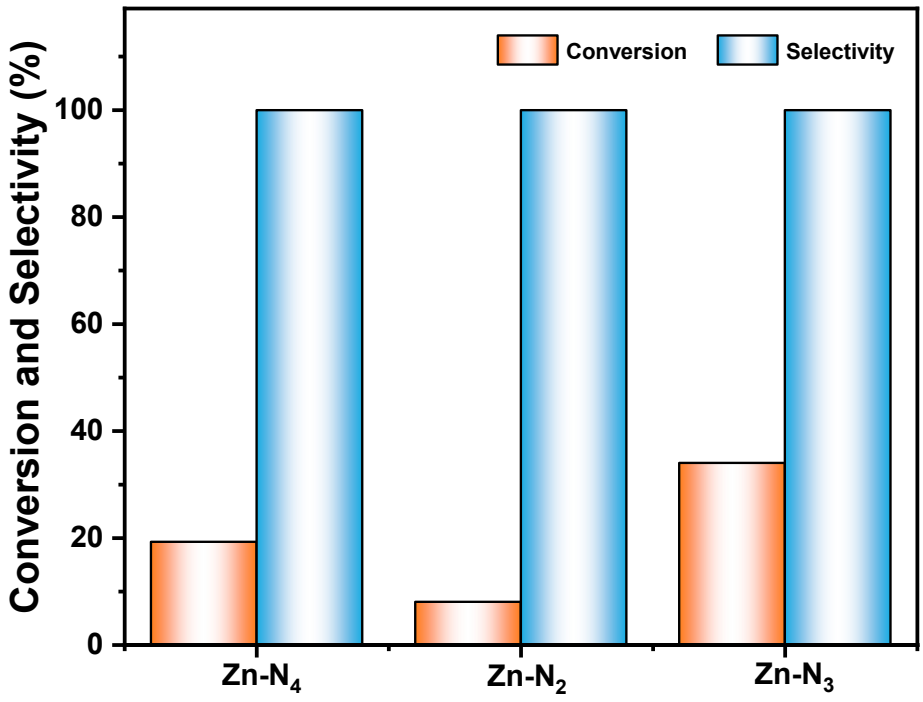

Figure S17. Catalytic intramolecular hydroamination of 2-(2-phenylethynyl)aniline over

various Zn-N_x SACs. **Reaction conditions:** 0.05 mmol of 2-(2-phenylethynyl)aniline, 2 mL of toluene, 10 mg of catalyst, 373 K, 6 h, under atmospheric N_2 atmosphere.

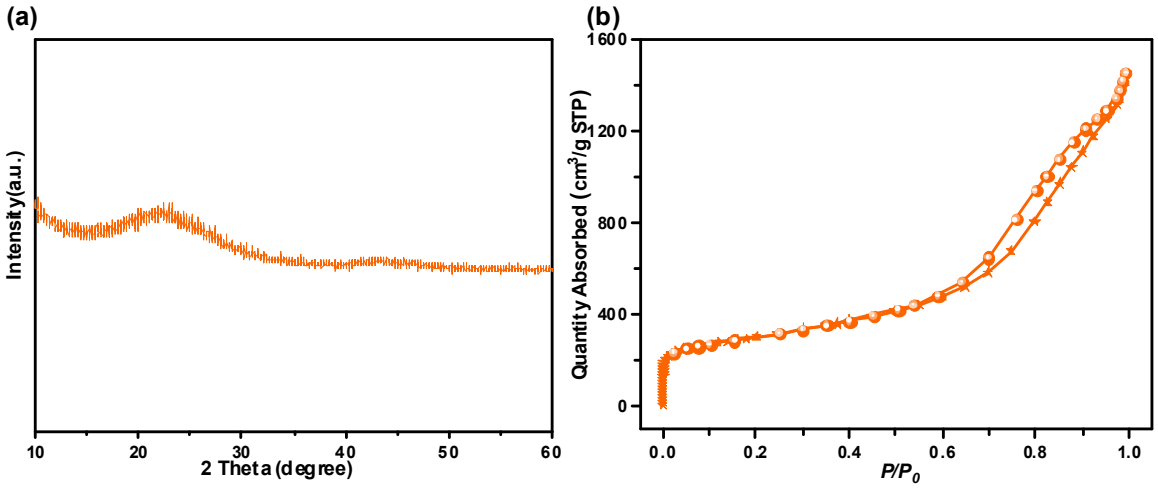

Figure S18. XRD pattern (a) and N_2 adsorption-desorption isotherms at 77 K (b) of the used Zn-N_2P SAC.

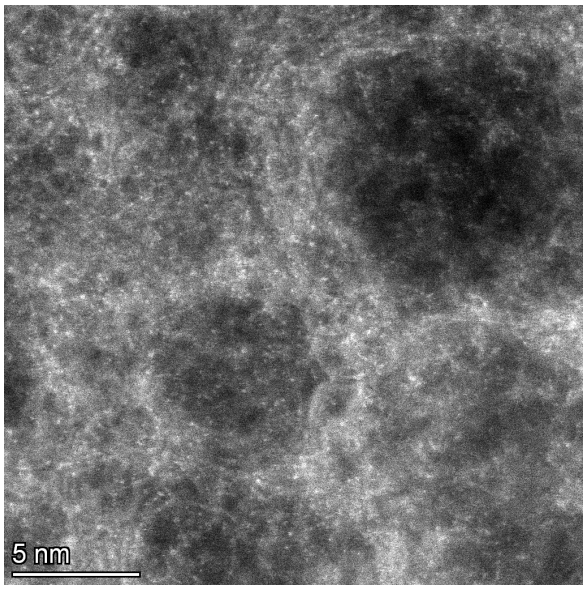

Figure S19. HAADF-STEM image of the used Zn-N_2P SAC.

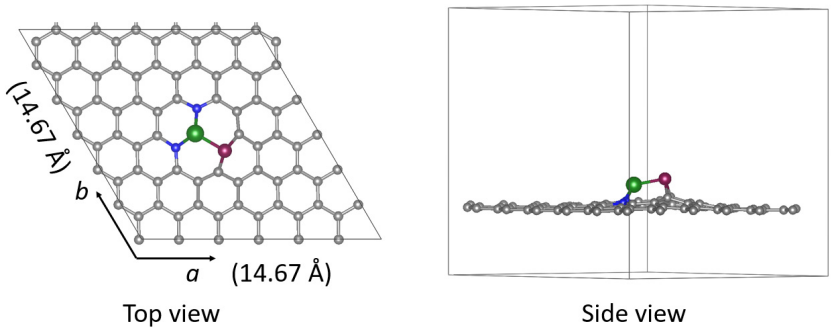

Figure S20. Optimized structure of Zn-N_2P model visualized from the top and the side.

The binding energies of Zn atoms in the Zn-N_xY models (Y = N, P, B, S) were calculated to evaluate their stabilities by

$$E_{ads} = E_{Zn-N_xY} - E_{Zn} - E_{N_xY}$$

where the E_{Zn} represent the energy for single Zn atom with the reference energy of Zn bulk, and E_{N_xY} is for the energy of N_xY fragment without optimization. The results show that the Zn-N_4 model has the lowest adsorption energy of -4.24 eV, followed by Zn-N_3 with a value of -2.20 eV.

Structurally, the S-doping into the Zn-N_3 model leads to a different configuration as compared to Zn-N_2P, since the S and Zn atoms are located at the opposite sides of the planar sheet in the most stable Zn-N_2S. Therefore, the Zn atom actually anchors to only two N atoms in Zn-N_2S with coordination number of 2, and the binding energy is -1.91 eV, weaker than that of -2.64 eV in Zn-N_2P. For Zn-N_2B model, the Zn atom has a very weak interaction with the planar sheet in Zn-N_2B model since its binding energy is only -0.46 eV, suggesting the Zn-N_2B model is less stable.

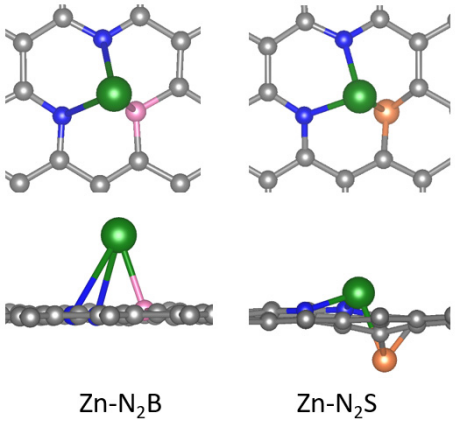

Figure S21. Optimized structures of Zn-N_2B and Zn-N_2S models.

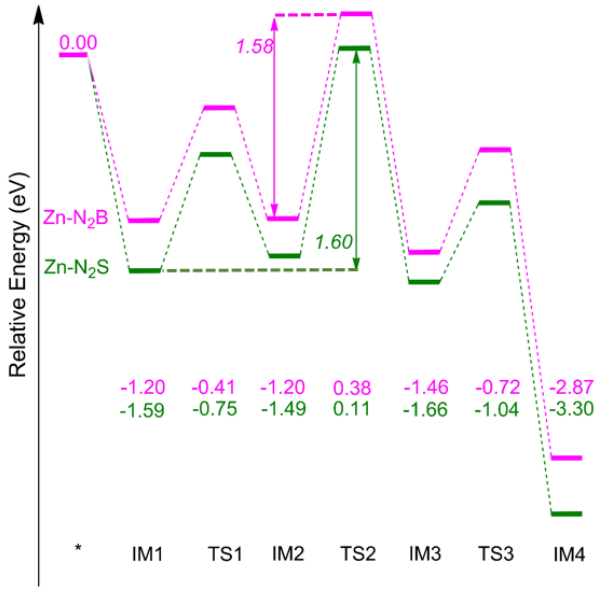

Figure S22. Reaction profile for intramolecular hydroamination of 2-(2-phenylethynyl)aniline using Zn-N_2B and Zn-N_2S catalysts.

Analytical data of the products

Indole

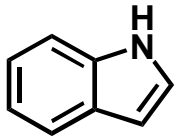

^{1}H NMR (600 MHz, DMSO) δ 11.06 (s, 1H), 7.53 (d, J = 7.9 Hz, 1H), 7.41 (dd, J = 8.1, 0.7 Hz, 1H), 7.30 (t, J = 2.8 Hz, 1H), 7.07 (s, 1H), 6.98 (s, 1H), 6.41 (s, 1H).

^{13}C NMR (151 MHz, DMSO) δ 136.41, 128.17, 125.62, 121.40, 120.53, 119.29, 111.90, 101.52.

2-phenyl-1H-indole

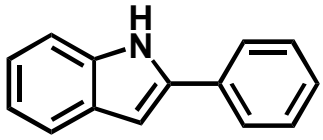

^{1}H NMR (600 MHz, DMSO) δ 11.50 (s, 1H), 7.86 - 7.82 (m, 2H), 7.50 (d, J = 7.8 Hz, 1H), 7.42 (t, J = 7.8 Hz, 2H), 7.38 (d, J = 8.0 Hz, 1H), 7.27 (s, 1H), 7.07 (s, 1H), 6.97 (s, 1H), 6.86 (d, J = 1.7 Hz, 1H).

^{13}C NMR (151 MHz, DMSO) δ 138.78, 138.30, 133.39, 130.04, 129.80, 128.53, 126.14, 122.72, 121.20, 120.52, 112.46, 99.83.

2-p-Tolyl-1H-indole

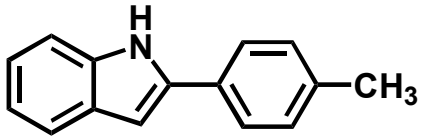

^{1}H NMR (600 MHz, DMSO) δ 11.45 (s, 1H), 7.72 (d, J = 8.1 Hz, 2H), 7.48 (d, J = 7.8 Hz, 1H), 7.36 (d, J = 8.0 Hz, 1H), 7.23 (d, J = 7.9 Hz, 2H), 7.05 (s, 1H), 6.96 (d, J = 7.2 Hz, 1H), 6.79 (d, J = 1.6 Hz, 1H), 2.30 (s, 3H).

^{13}C NMR (151 MHz, DMSO) δ 138.49, 137.71, 137.46, 130.17, 129.41, 125.62, 122.02, 120.57, 119.99, 111.91, 98.75, 21.51.

2-(4-chlorophenyl)-1H-indole

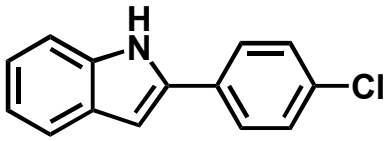

^{1}H NMR (600 MHz, DMSO) δ 11.60 (s, 1H), 7.90 - 7.88 (m, 2H), 7.55 - 7.42 (m, 4H), 7.08 (ddd, J = 56.5, 7.9, 4.0 Hz, 2H), 6.94 (d, J = 1.4 Hz, 1H).

^{13}C NMR (151 MHz, DMSO) δ 138.39, 137.52, 132.93, 132.30, 130.06, 129.71, 127.77, 123.04, 121.34, 120.68, 112.52, 100.49.

2-(4-fluorophenyl)-1H-indole

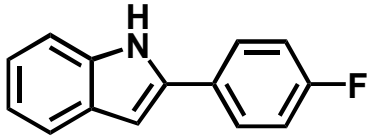

^{1}H NMR (600 MHz, DMSO) δ 11.54 (s, 1H), 7.94 - 7.87 (m, 2H), 7.53 (d, J = 7.8 Hz, 1H), 7.41 (d, J = 8.1 Hz, 1H), 7.35 - 7.26 (m, 2H), 7.13 - 7.08 (m, 1H), 7.01 (dd, J = 11.0, 3.9 Hz, 1H), 6.87 (d, J = 1.7 Hz, 1H).

^{13}C NMR (151 MHz, DMSO) δ 161.23, 137.61, 137.21, 129.13, 127.47, 122.06, 120.51, 119.90, 116.37, 116.22, 111.76, 99.15.

2-(4-methoxyphenyl)-1H-indole

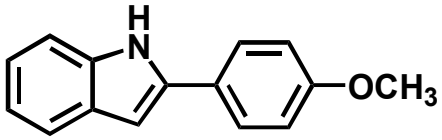

^{1}H NMR (600 MHz, DMSO) δ 11.42 (s, 1H), 7.80 (d, J = 8.8 Hz, 2H), 7.50 (s, 1H), 7.38 (dd, J = 8.0, 0.5 Hz, 1H), 7.06 (s, 1H), 7.03 (d, J = 8.8 Hz, 2H), 6.98 (s, 1H), 6.76 (d, J = 1.5 Hz, 1H), 3.81 (s, 3H).

^{13}C NMR (151 MHz, DMSO) δ 159.28, 138.26, 137.42, 129.33, 126.85, 125.40, 121.54, 120.16, 119.73, 114.85, 111.57, 97.83, 55.70.

5-chloro-2-phenyl-1H-indole

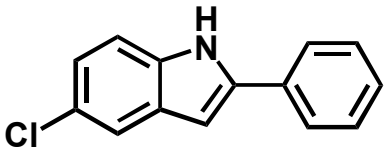

^{1}H NMR (600 MHz, DMSO) δ 11.77 (s, 1H), 7.86 (d, J = 7.3 Hz, 2H), 7.57 (d, J = 1.9 Hz, 1H), 7.47 (t, J = 7.8 Hz, 2H), 7.42 (d, J = 8.6 Hz, 1H), 7.34 (t, J = 7.4 Hz, 1H), 7.10 (dd, J = 8.6, 2.0 Hz, 1H), 6.88 (d, J = 1.1 Hz, 1H).

^{13}C NMR (151 MHz, DMSO) δ 139.80, 136.03, 132.16, 130.25, 129.43, 128.31, 125.63, 124.38, 121.93, 119.56, 113.23, 98.84.

Figures S23-S29. ^{1}H and ^{13}C NMR spectra of coupling products.

Figure S23. ^{1}H and ^{13}C NMR spectra for Indole.

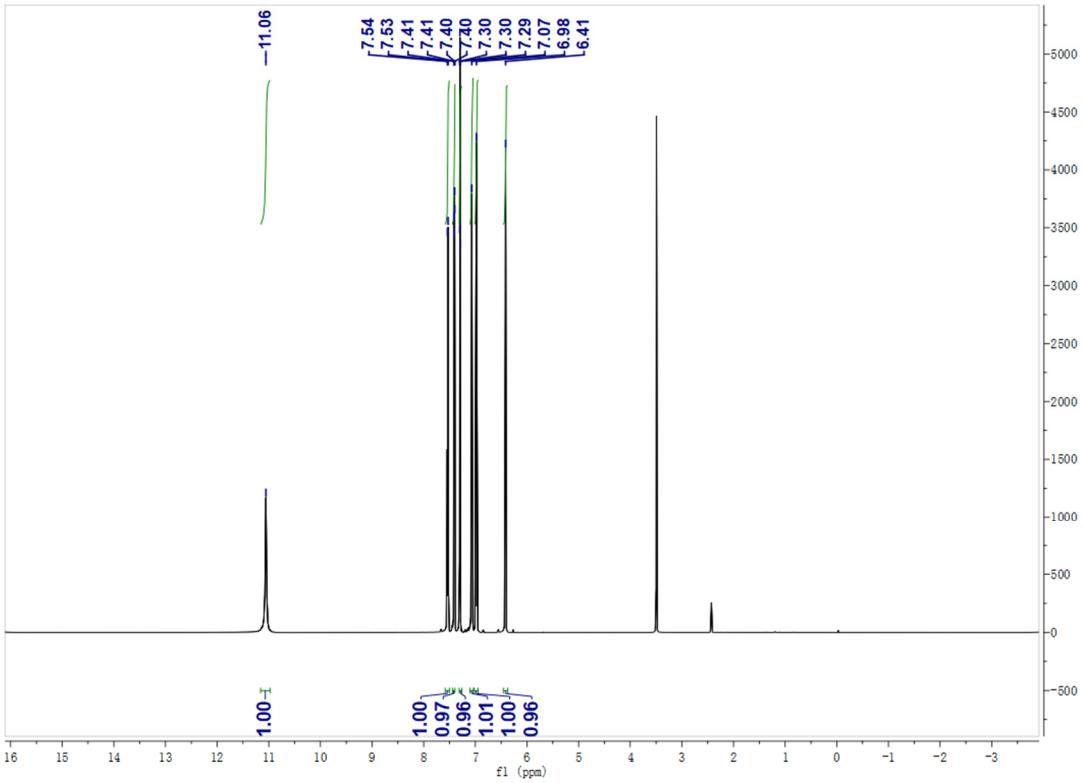

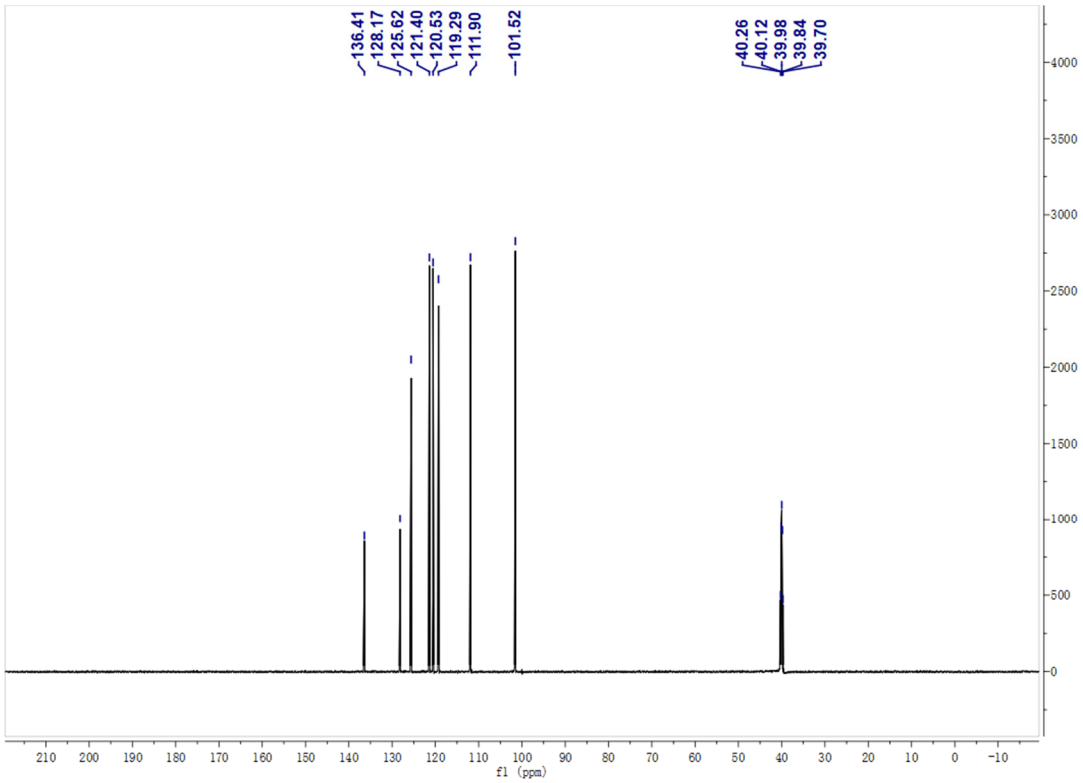

Figure S24. ^{1}H and ^{13}C NMR spectra for 2-phenyl-1H-indole.

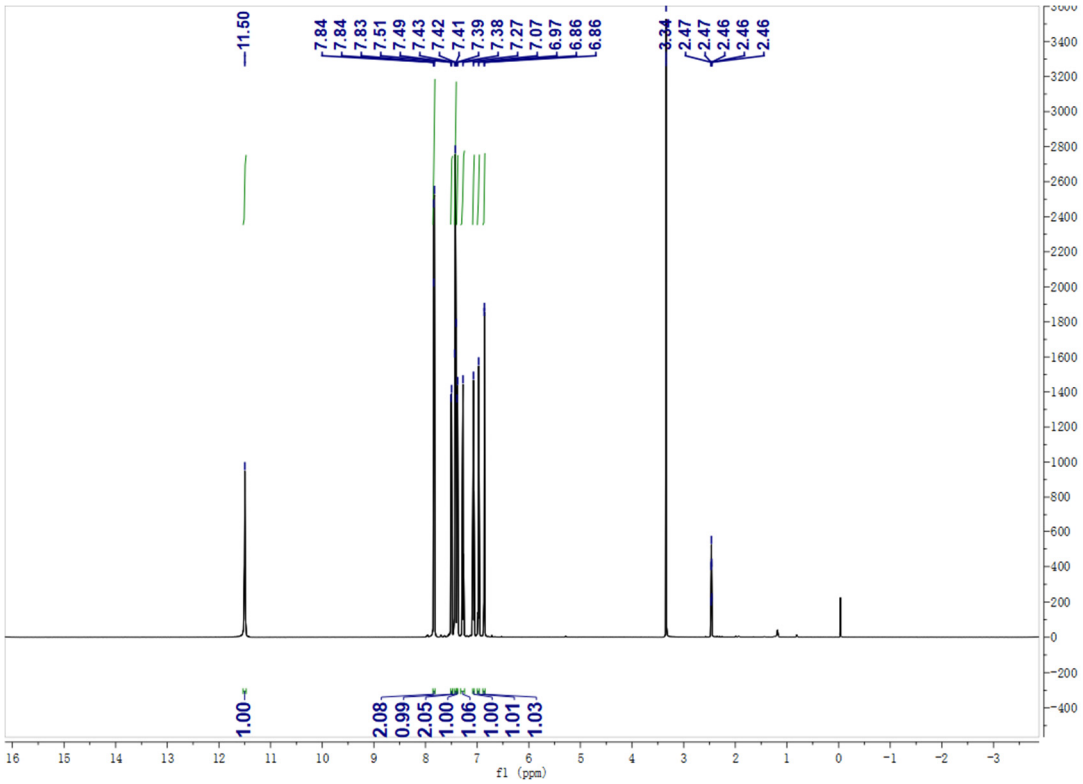

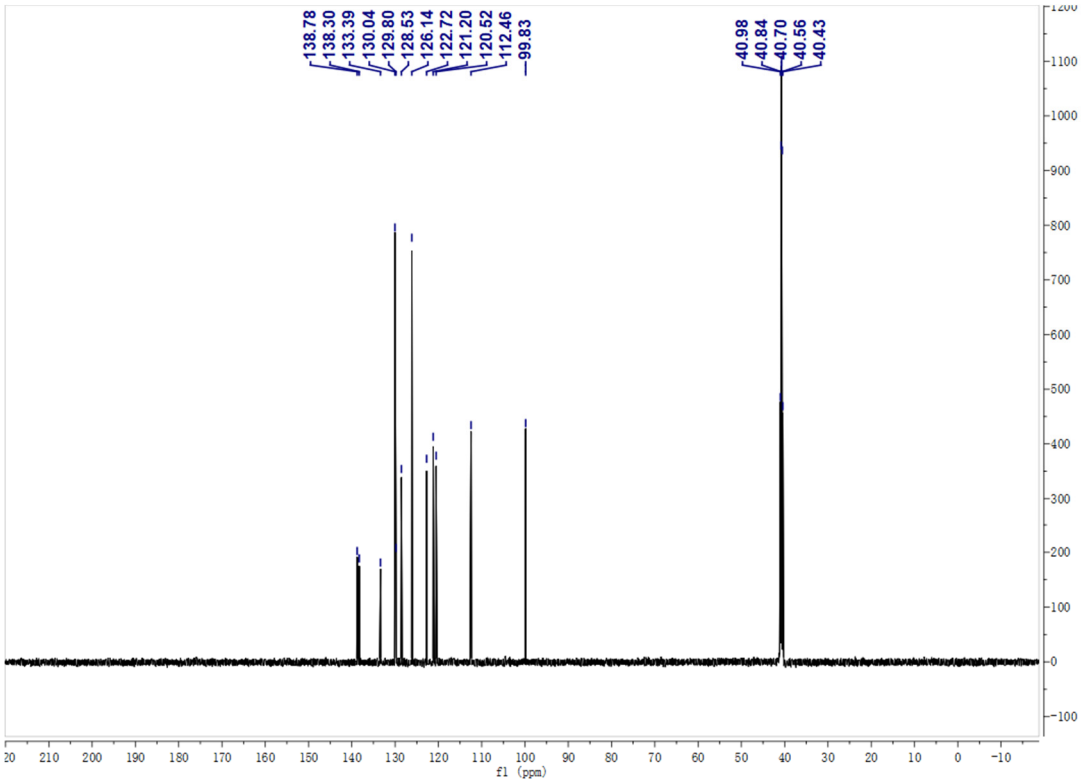

Figure S25. ^{1}H and ^{13}C NMR spectra for 2-p-Tolyl-1H-indole.

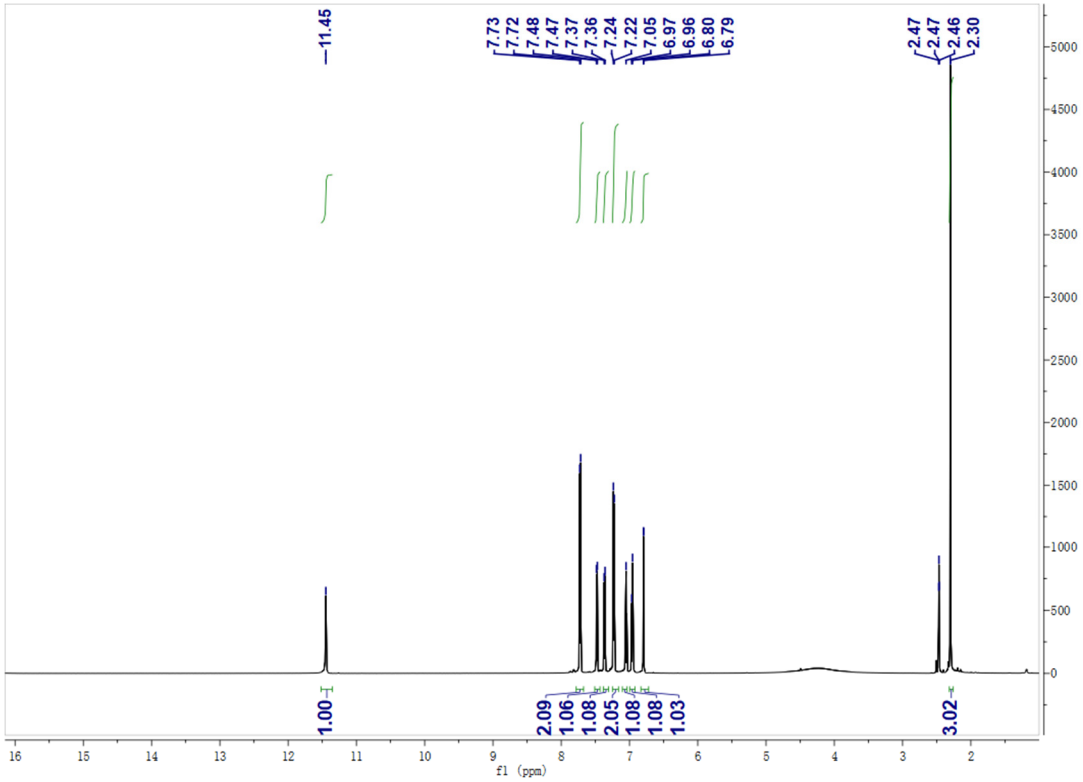

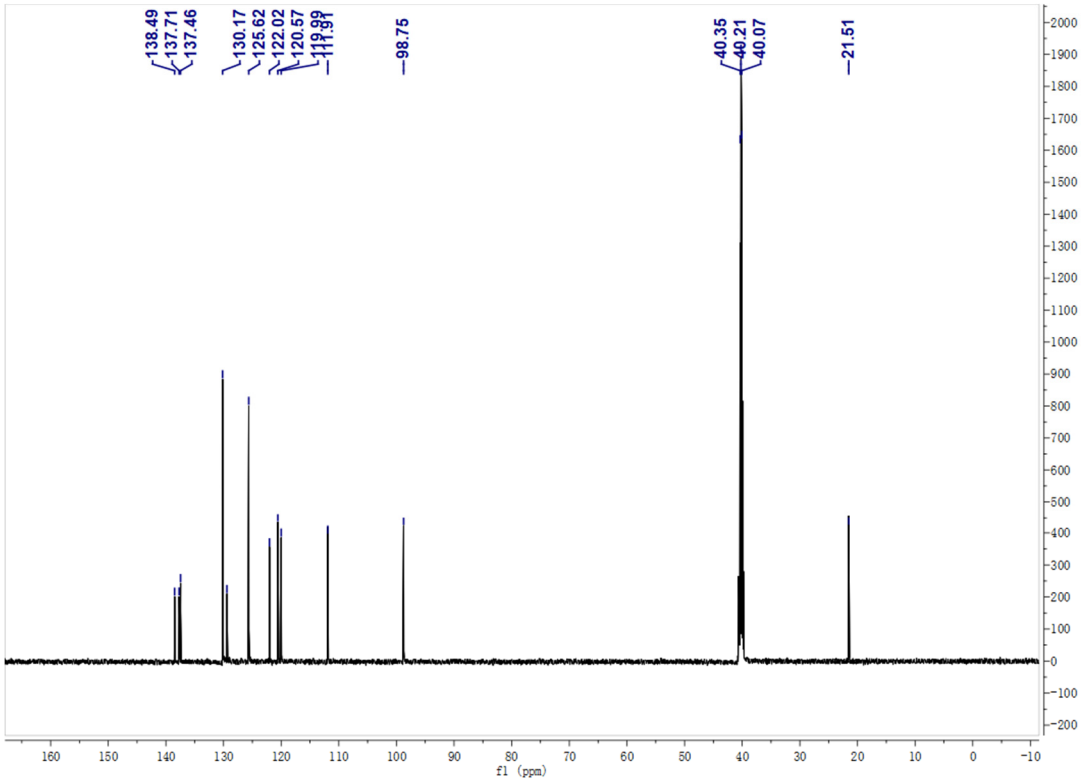

Figure S26. ^{1}H and ^{13}C NMR spectra for 2-(4-chlorophenyl)-1H-indole.

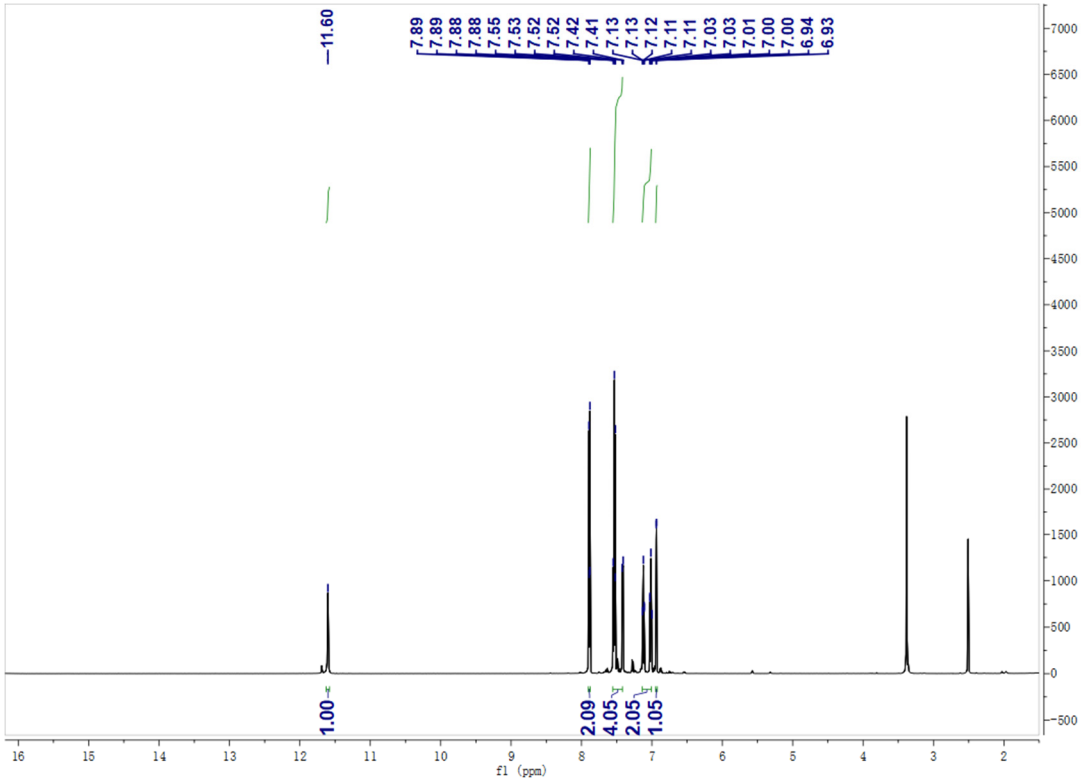

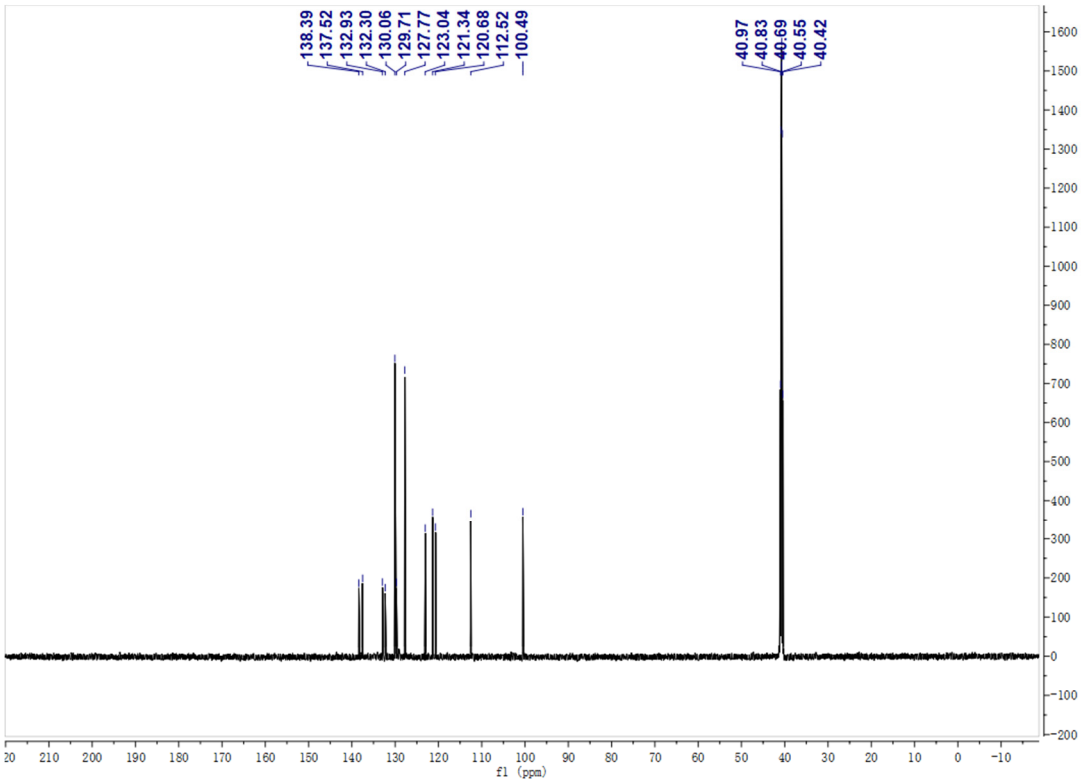

Figure S27. ^{1}H and ^{13}C NMR spectra for 2-(4-fluorophenyl)-1H-indole.

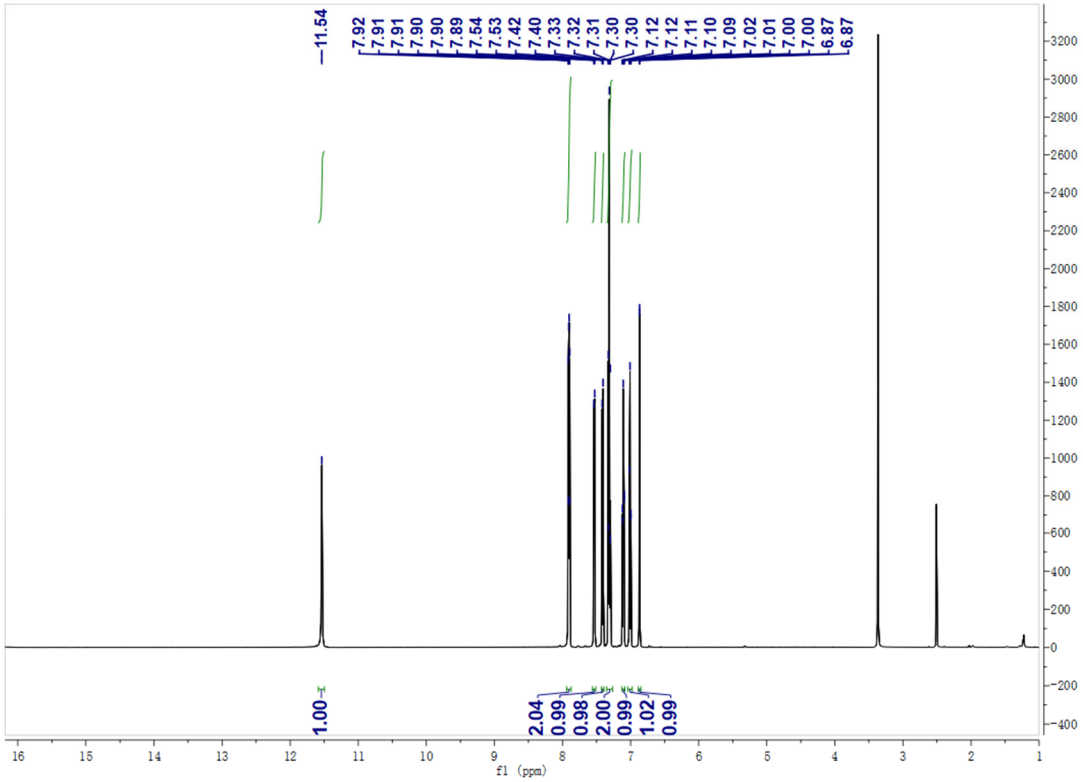

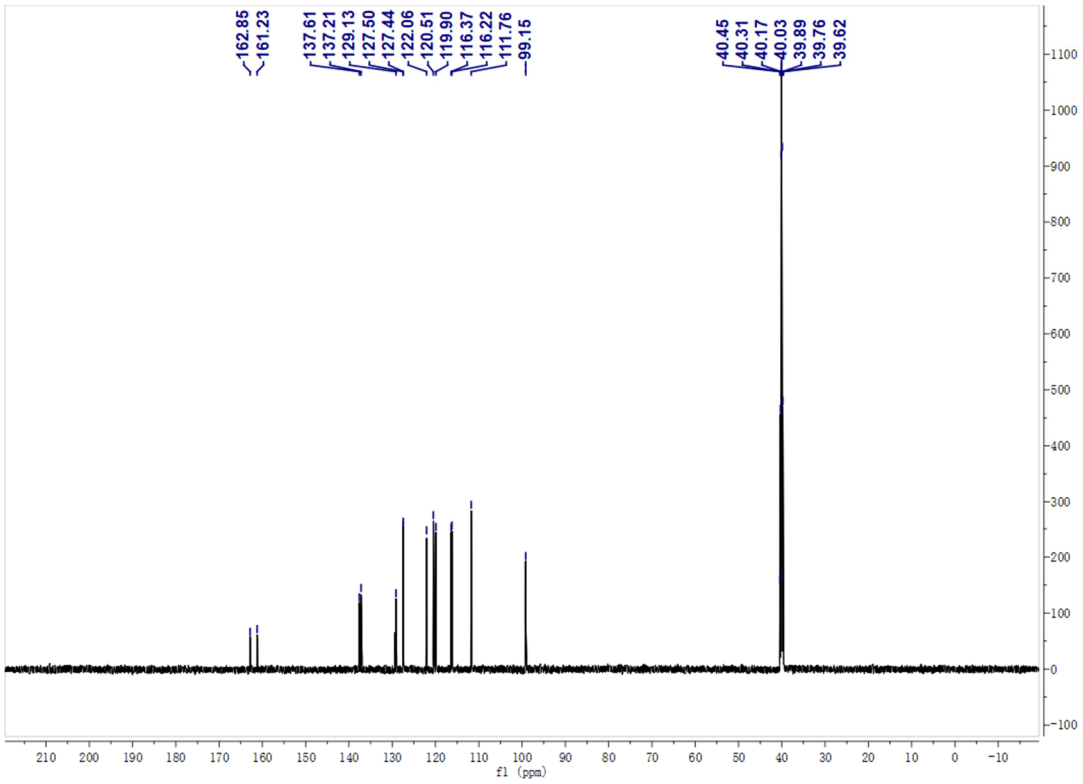

Figure S28. ^{1}H and ^{13}C NMR spectra for 2-(4-methoxyphenyl)-1H-indole.

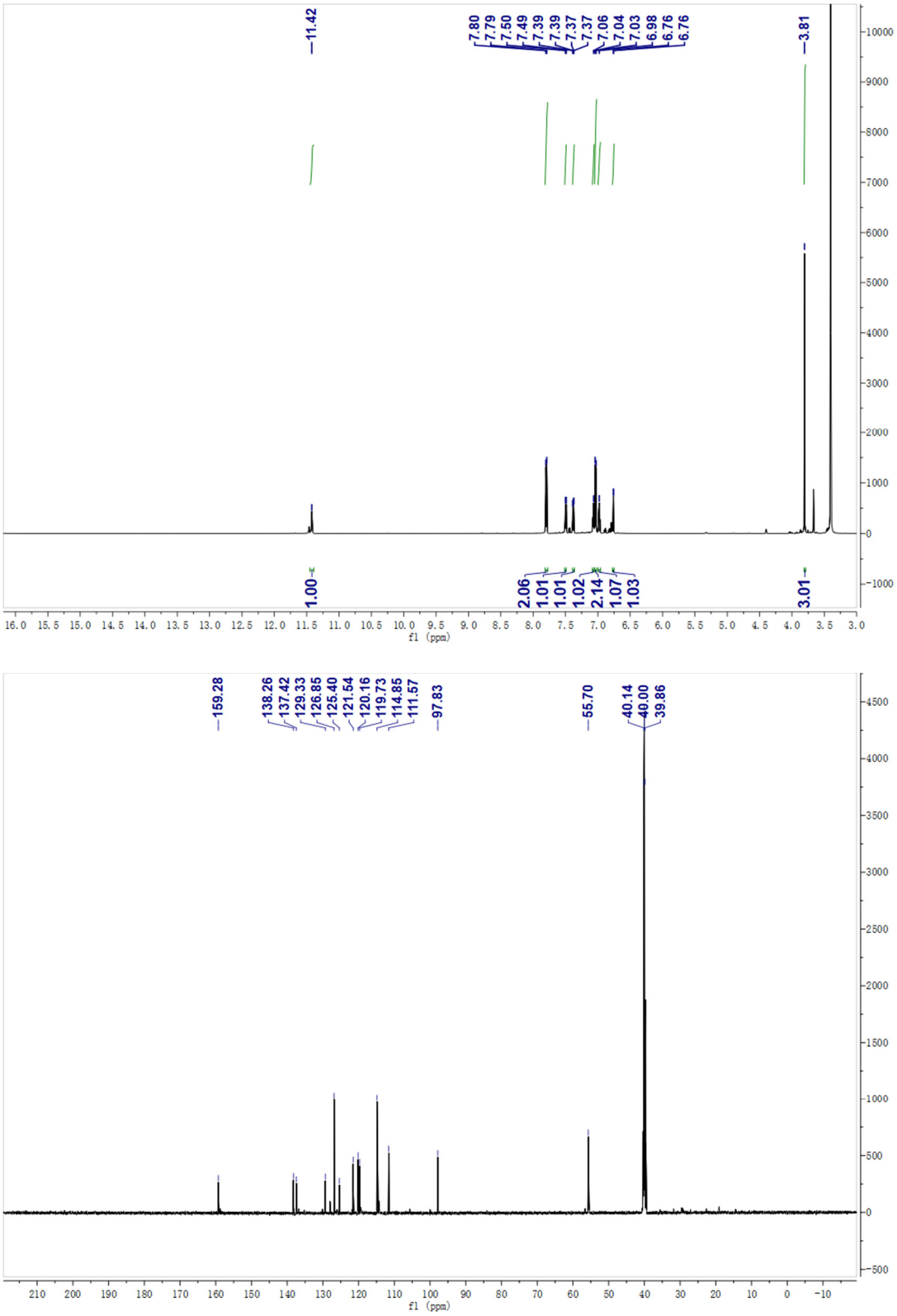

Figure S29. ^{1}H and ^{13}C NMR spectra for 5-chloro-2-phenyl-1H-indole.

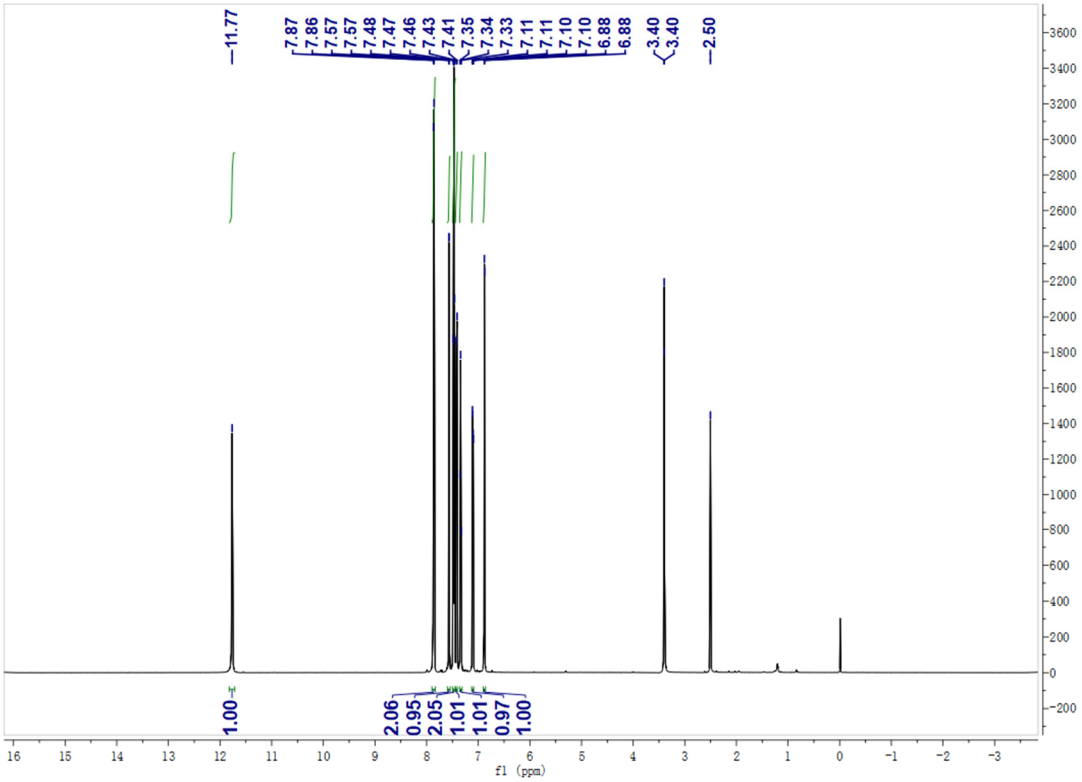

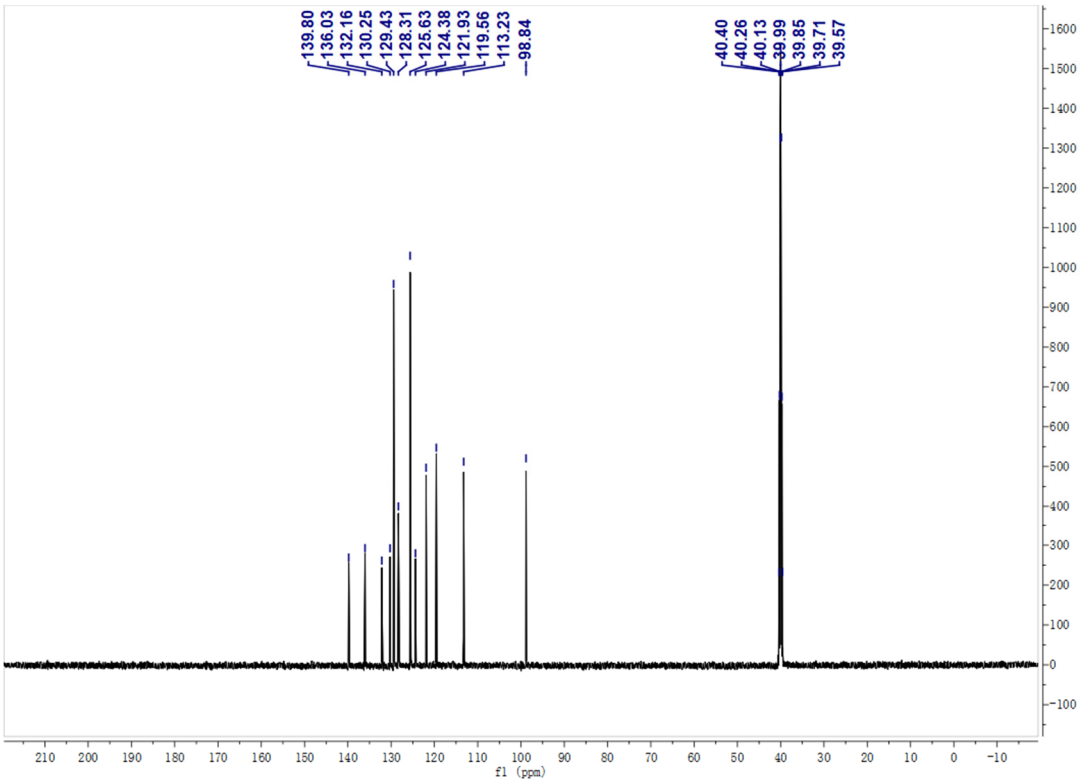

References

s1. G. Kresse and J. Hafner, *Phys. Rev. B.* **1993**, *47*, 558–561.

s2. G. Kresse and J. Hafner, *Phys. Rev. B.* **1994**, *49*, 14251–14269.

s3. G. Kresse and J. Furthmüller, *Phys. Rev. B.* **1996**, *54*, 11169–11186.

s4. G. Kresse and J. Furthmüller, *Comput. Mater. Sci.* **1996**, *6*, 15–50.

s5. J. P. Perdew, K. Burke and M. Ernzerhof, *Phys. Rev. B.* **1996**, *77*, 3865–3868.

s6. S. Grimme, *J. Comput. Chem.* **2006**, *27*, 1787–1799.

s7. G. Henkelman, B. P. Uberuaga and H. Jónsson, *J. Chem. Phys.* **2000**, *113*, 9901–9904.

s8. Z. Tian, D.-L. Chen, T. He, P. Y. Yang, F.-F. Wang, Y. J. Zhong and W. D. Zhu, *J. Phys. Chem. C* **2019**, *123*, 22114–22122.

s9. K. Gray, M.J. Page, J. Wagler and B.A. Messerle, O*rganometallics*, 2012, **31**, 6270−6277.

s10. E.D. Finashina, O.P. Tkachenko, A.Y. Startseva, E.A. Redina, V.G. Krasovsky, L.M. Kustov and I.P. Beletskaya, *Russ. Chem. Bull.*, 2015, **64**, 2821–2829.

s11. S. Liang, L. Hammond, B. Xu and G.B. Hammond, *Adv. Synth. Catal*., 2016, **358**, 3313–3318.

s12. J. Kwon, J. Chung, S. Byun and B.M. Kim, *Asian J. Org. Chem*., 2016, **5**, 470–476.

s13. P. Rubio-Marqués, M.A. Rivero-Crespo, A. Leyva-Pérez and A. Corma, *J. Am. Chem. Soc.*, 2015, **137**, 11832–11837.

s14. T. Khandelia, S. Ghosh, P. Panigrahi, R. Shome, S.S. Ghosh and B.K. Patel, *J. Org. Chem.*, 2021, **86**, 16948−16964.

s15. R. Jia, B. Li, X. Zhang and X. Fan, *Org. Lett.*, 2020, **22**, 6810–6815.

s16. Y. Kitazawa, R. Takita, K. Yoshida, A. Muranaka, S. Matsubara and M. Uchiyama, *J. Org. chem*., 2017, **82**, 1931–1935.

s17. M. Zille, A. Stolle, A. Wild and U.S. Schubert, *RSC Adv.*, 2014, **4**, 13126–13133.

s18. P. Rubio-Marqués, M.A. Rivero-Crespo, A. Leyva-Pérez and A. Corma, *J. Am. Chem. Soc.*,

2015, **137**, 11832–11837.

s19. A.K. Cook and C. Copéret, *Organometallics*, 2018, **37**, 1342–1345.